ELSEVIER

Catalysis Today 67 (2001) 15–32

CATALYSIS TODAY

www.elsevier.com/locate/cattod

PEM fuel cell as a membrane reactor

Tony Thampan [a], Sanjiv Malhotra [b], Jingxin Zhang [a], Ravindra Datta [a,*]

[a] *Department of Chemical Engineering, Fuel Cell Center, Worcester Polytechnic Institute, Worcester, MA 01609, USA*
[b] *H Power Corp., 60 Montgomery Street, Belleville, NJ 07109, USA*

Abstract

The H_2–O_2 proton-exchange membrane (PEM) fuel cell, among numerous other potential applications now slated to provide the motive power for the next generation of highly efficient and largely pollution-free automobiles, is an incomparable membrane reactor, comprising an exquisitely designed membrane-electrode-assembly (MEA), a five-layer composite of two gas-diffusion layers, two supported-catalyst layers, and a PEM. The device allows catalytic reaction and separation of hydrogen and oxygen as well as protons and electrons. This paper describes the structure and performance of the PEM fuel cell considered as a membrane reactor and develops an analytical transport–reaction model that, despite some assumptions, captures the essential features of the device very well. The key assumptions are that transport resistance as well as ohmic drop are negligible in the catalyst layer. While the latter is defensible, the former causes deviations at high current densities. Nonetheless, the model predicts the fuel cell performance well with parameter values reported in the literature. © 2001 Published by Elsevier Science B.V.

Keywords: Proton-exchange membrane; Membrane-electrode-assembly; Transport–reaction model; Fuel cell

1. Introduction

Fuel cells offer the potential of revolutionizing electrical energy production by affording highly efficient and largely pollution-free power generation systems for both transportation and stationary applications [30,46]. Proton-exchange membrane (PEM) fuel cells [27], operating on H_2 and O_2 (from air), are the focus at this time, although other fuel cells, namely, molten carbonate fuel cells (MCFCs), solid-oxide fuel cells (SOFCs) and direct methanol fuel cells (DMFCs) also hold promise for various applications [7,34]. The PEM fuel cell is particularly attractive because of mild operating conditions (50–80°C temperature, 1–3 atm pressure), low Pt loadings, relative robustness, long life, and the fact that all of its components are solid. It comprises an intricate membrane-electrode-assembly (MEA), a five-layer composite of two gas-diffusion layers that allow simultaneous transport of gases and water while collecting current, two three-phase supported-catalyst (typically Pt/C) layers, and a PEM, typically a perfluorosulfonic acid (PFSA) polymer such as Nafion®. It is, in fact, a superb example of a catalytic membrane reactor performing a variety of reactions and separations. The MEA nanostructure has evolved over a considerable period of time to now provide exceptional performance. Thus, many of the fabrication issues for attaining superior performance have been resolved. However, before wide-spread usage of PEM fuel cells becomes a reality, there are still a number of technical/cost challenges that remain to be addressed.

A key limitation is that the proton conductivity of the PEM is strongly dependent upon its water content,

* Corresponding author. Tel.: +1-508-8315250; fax: +1-508-8315853.
E-mail address: rdatta@wpi.edu (R. Datta).

0920-5861/01/$ – see front matter © 2001 Published by Elsevier Science B.V.
PII: S0920-5861(01)00278-4

Nomenclature

a_i	activity of species i
a_w	activity, or relative humidity RH, of water $= p_w/p_w^0$
a_α	mean pore radius of porous layer α (nm)
A	geometric area of PEM in fuel cell
A_ρ	pre-exponential factor of reaction ρ
$A_i^{z_i}$	species i with charge z_i
$B_{0\alpha}$	d'Arcy permeability of layer α (cm^2)
c	total concentration of mixture $= \sum_i c_i$ (mol/cm^3)
$c_{HA,0}$	concentration of membrane acid groups $= 1/\lambda \bar{V}_2$ (mol/cm^3 pore solution)
c_{iS}	concentration of species i in region S
c_{iT}	concentration of species i in region T
$c_{i\alpha}$	concentration of species i in layer α (mol/cm^3)
C	BET constant
d_M	catalyst metal microcrystallite diameter (nm)
D_{ij}	mutual diffusion coefficient for species i and j (cm^2/s)
D_{iL}	liquid-phase diffusion coefficient of species i (cm^2/s)
D_{iG}^e	effective gas-phase diffusion coefficient of species i in the gas-diffusion backing (cm^2/s)
D_{ij}^e	effective mutual diffusion coefficient of species i and $j = K_1 D_{ij}$ (cm^2/s)
D_{ij}^{e0}	pressure independent effective binary diffusion coefficient of species i and $j = pD_{ij}^e$ (bar cm^2/s)
D_{iK}^e	effective Knudsen diffusion coefficient of species i (cm^2/s)
D_{iM}^e	effective diffusion coefficient for interaction of species i and matrix M $= K_0 D_{iM}$ (cm^2/s)
$D_{i\alpha}^e$	effective diffusion coefficient of species i in layer α (cm^2/s)
E_{A,Φ_0}	effective activation energy of $i_{A,0}$ or $\vec{k}^*_{A,\Phi_0}$
E_μ	activation energy for viscosity (kJ/mol)
F	Faraday's constant, 96,487 C/eq
F_T	volumetric flow rate in anode
HA	acid group (e.g., $-SO_3H$) in membrane
ΔH^0	enthalpy change for proton solvation (kJ/mol)
$\Delta \vec{H}^{\pm 0}_{\rho T,\Phi=0}$	standard enthalpy change of activation for forward elementary reaction ρ
i	fuel cell current density (A/cm^2 of geometric electrode area)
i_A	anodic current density (A/cm^2 of geometric electrode area)
i_0	exchange current density (A/cm^2 of geometric electrode area)
$i_{A,L}$	anodic limiting current density (A/cm^2 of geometric electrode area)
$i_{A,0}$	anodic exchange current density (A/cm^2 of geometric electrode area)
i_C	cathodic current density (A/cm^2 of geometric electrode area)
$i_{C,L}$	cathodic limiting current density (A/cm^2 of geometric electrode area)
$i_{C,0}$	cathodic exchange current density (A/cm^2 of geometric electrode area)
i^*	current density (A/cm^2 of metal catalyst surface)
i_0^*	exchange current density (A/cm^2 of metal catalyst surface)
$i^*_{A,0}$	anodic exchange current density (A/cm^2 of metal catalyst surface)
$i^*_{C,0}$	cathodic exchange current density (A/cm^2 of metal catalyst surface)
k_B	Boltzmann constant
k_A^*	effective rate constant of overall anode reaction
$\vec{k}^*_{A,\Phi_0}$	rate constant of anode reaction at equilibrium electrode potential Φ_0
k_C^*	effective rate constant of overall cathode reaction
$\vec{k}^*_{C,\Phi_0}$	rate constant of anode reaction at equilibrium electrode potential Φ_0
$\vec{k}^*_\rho$	rate constant of forward elementary reaction ρ (s^{-1})
$\overleftarrow{k}^*_\rho$	rate constant of reverse elementary reaction ρ (s^{-1})

$\vec{k}^*_{\rho,\Phi_0}$	rate constant of forward elementary reaction ρ at equilibrium electrode potential Φ_0 (s^{-1})
$K_{A,C}$	equilibrium constant for proton solvation in terms of concentrations
K_ρ	equilibrium constant of reaction ρ
K_{ρ,Φ_0}	equilibrium constant of reaction ρ at equilibrium electrode potential Φ_0
$K_{0\alpha}$	dusty-gas constant of layer α for effective Knudsen diffusion coefficient (cm)
$K_{1\alpha}$	dusty-gas constant of layer α for effective binary diffusion coefficient
L_α	thickness of layer α
m_I	ionomer loading in catalyst layer (g metal/cm^2 geometric electrode area)
m_M	catalyst loading (g metal/cm^2 geometric electrode area)
n	total number of species
n_w	total number of water layers sorbed on the pore surface
n_ρ	number of electrons participating in reaction ρ
N_i	flux of species i (mol/cm^2 geometric electrode area)
p	total pressure (bar)
p_i	partial pressure of species i (bar)
p_S	total pressure in cathode chamber (bar)
p_T	total pressure in anode chamber (bar)
p^0_w	vapor pressure of water (bar)
P	power density (W/cm^2 geometric electrode area)
$P_{i\alpha}$	permeability of layer α for species $i = D_{i\alpha}\kappa_{i\alpha}/L_\alpha$ (cm/s)
q	Bruggeman or critical exponent = 1.5
q_I	ionomer loading in catalyst layer (cm^3 ionomer/cm^3 void volume)
q_α	liquid loading of layer α (cm^3 liquid/cm^3 void volume)
r	net rate of reversible reaction $\rho = \vec{r}_\rho - \overleftarrow{r}_\rho$ (mol/cm^3 catalyst particles s)
$\vec{r}_0$	rate of forward reaction under open circuit conditions (mol/cm^3 catalyst particles s)
r^*_A	net rate of anodic reaction (mol/cm^2metal catalyst area s)
r^*_C	net rate of cathodic reaction (mol/cm^2 metal catalyst area s)
r^*	net rate of reversible reaction $\rho = \vec{r}^*_\rho - \overleftarrow{r}^*_\rho$ (mol/cm^2 metal catalyst area s)
$r_{\rho 0}$	reaction rate at open circuit
R	universal gas constant, 8.3143 J/mol K
R_I	interfacial resistance ($\Omega\,cm^2$)
s	surface coordination number
S	catalyst site
S_M	specific surface area of metal crystallites (cm^2/g metal)
S_S	specific surface area of carbon support particles (cm^2/g carbon)
$\Delta\vec{S}^{\pm 0}_{T,\Phi=0}$	standard entropy change of activation for forward elementary reaction ρ
T	temperature (K)
V	fuel cell potential $= \phi_{M,C} - \phi_{M,A}$ (V)
V_0	open circuit potential $= \Phi_{0,C} - \Phi_{0,A}$ (V)
$\bar{V}_i$	partial molar volume of species i (cm^3/mol)
W	expression given by Eq. (6) (dimensionless)
z	coordinate
z_i	charge number of species i

Greek letters

α	degree of acid group dissociation
$\vec{\alpha}_A$	effective transfer coefficient of overall anode reaction = $\frac{1}{2}$
$\vec{\alpha}_C$	effective transfer coefficient of overall cathode reaction = 1
β_ρ	symmetry factor of elementary reaction $\rho = \frac{1}{2}$
γ_M	roughness factor (cm^2 Pt/cm^2 geometric electrode area)
$\gamma^\pm$	activity coefficient of transition-state complex
δ	ratio of mutual to matrix effective diffusion coefficients, $D^e_{H^+w}/D^e_{H^+M}$
ε	volume fraction of water in hydrated membrane, or wet porosity

ε_0	percolation threshold volume fraction of water in hydrated membrane
ε_α	porosity for porous layer α
η	overpotential $= \Phi - \Phi_0$ (V)
η_A	anodic overpotential (V)
η_C	cathodic overpotential (V)
θ_i	fraction of surface sites occupied by species i
κ	transmission coefficient
$\kappa_{i\alpha}$	partition coefficient of species i in layer $\alpha = (c_{i\alpha}/c_{iG})_{eq}$
λ	water loading, number of water molecules per $-SO_3H$ group
λ_m	water loading at monolayer coverage, number of water molecules per $-SO_3H$ group
λ_i^0	equivalent conductance for ionic species i at infinite dilution (S cm^2/equiv.)
μ	fluid mixture viscosity (g/cm s)
μ_i	chemical potential of species i (J/mol)
μ_i^e	electrochemical potential of species i (J/mol)
$\nu_{\rho i}$	stoichiometric coefficient of species i in reaction ρ
$\nu_{\rho e^-}$	stoichiometric coefficient of electrons in reaction ρ
ρ_I	ionomer density (g/cm^3)
σ	effective conductivity of PEM (layer B) (S/cm)
τ_α	tortuosity factor for porous layer α
ϕ	inner potential (V)
φ_I	fraction of accessible catalyst surface participating in electrocatalysis
φ_M	fraction of metal crystallite surface that is accessible
Φ	electrode potential (V)
Φ_0	equilibrium electrode potential (V)
Φ_0^0	standard equilibrium electrode potential for unit activities (V)
ω_M	metal catalyst mass fraction (g metal/g catalyst particles)

Subscripts and superscripts

A	layer A (anode electrocatalyst)
B	layer B (PEM)
C	layer C (cathode electrocatalyst)
d	diluent gas
D	layer D (anode gas-diffusion backing)
E	layer E (cathode gas-diffusion backing)
G	gas phase
H^+	H_3O^+
i	species i
I	ionomer
M	membrane
M	metal, membrane matrix
S	layer S (cathode chamber)
T	at constant temperature T
T	layer T (anode chamber)
w	water
0	open circuit conditions, dry membrane, reference, percolation threshold
298	at reference temperature, 298 K
α	generic layer
ρ	reaction ρ
Φ_0	at equilibrium electrode potential
$*$	per cm^2 metal area

calling for elaborate water management and limiting the practical operating temperature to 80°C to avoid membrane drying [56]. At these low operating temperatures, however, the Pt anode is particularly susceptible to poisoning by even traces of CO in the anode H_2 feed [26]. However, since the storage and transportation of H_2 fuel at this time is impractical, conventional hydrocarbon or alcohol fuels must be locally reformed into a H_2 rich reformate gas that cannot be completely rid of CO. These catalytic processes, while well-developed for the industrial scale, have special requirements for fuel cell applications, thus offering innumerable challenges and opportunities in catalysis and reaction engineering [1,16]. Further, while the field of membrane reactors is of relatively recent vintage [15], fuel cells that possess many of the characteristics of membrane reactors have been around for well over a century. Thus, the field of membrane reactors can glean much from a careful study of this intriguing device.

The transport-kinetic modeling of fuel cell viewed as a catalytic membrane reactor [31] can shed further light on its design and operational factors, which is our objective here. Theoretical modeling of transport and reaction in fuel cells is challenging due to the complexity of the device and the numerous design

and operating parameters that can influence its performance. Models describing gas-diffusion electrodes and processes therein have been in development since 1960s [4,8,18,39]. Theoretical models of fuel cell performance tend to be either rather complex requiring considerable numerical effort, e.g., the comprehensive model of [5,6] or semi-empirical (e.g., [32]), or empirical [25]. The former are useful for a detailed mechanistic understanding of the factors that influence the fuel cell performance, while the latter are useful for simply predicting the overall performance of individual fuel cells in a stack [3]. Fuel cell models of varying degrees of detail and complexity are also given by Leddy and Vanderborgh [35], Ridge et al. [50], Fuller and Newman [20], Nguyen et al. [41], Springer et al. [53–55], Weisbrod et al. [59], and Perry et al. [47]. Our objective here is to develop an analytical model for PEM fuel cells by drawing parallels with membrane reactors and incorporating transport and reaction details coupled with judicious assumptions to provide an analytical model that is both simple to use as well as quite complete. Some aspects, e.g., MEA structure and electrocatalysis, are described in sufficient detail to introduce the catalytic membrane reactor technologist to the PEM fuel cell.

2. MEA nanostructure

The MEA structure comprising of gas-diffusion layer/anode catalyst/electrolyte/cathode catalyst/gas-diffusion layer composite is shown in Fig. 1. In a nutshell, H_2 is split into protons and electrons at the anode electrocatalyst. Protons find their way to the cathode through the PEM, while the electrons arrive at the cathode via the external circuit after performing useful work. Here, aided by electrode potential, the protons and electrons recombine with O_2 at the catalyst surface to form water. The MEA is sandwiched between two graphite plate current collectors, with machined microchannels, as in microchannel reactors [57], for gas distribution.

The gas-diffusion backing (GDB) (layers D and E) serves as the electron collector and a permeator for reactant gases as well as for liquid water. The PEM (layer B) requires water for effective proton transport, which limits the practical operating temperature of atmospheric fuel cells to about 80°C (when water vapor pressure is roughly half an atmosphere). However, if the pores of the gas-diffusion layers get filled with liquid water, transport of oxygen and hydrogen to the catalyst layers is impeded, severely limiting the fuel cell performance. This is avoided by imparting hydrophobicity to the gas-diffusion layers to allow gas and liquid phases to co-exist within pores. The gas-diffusion backing typically involves a carbon cloth, about 350 μm in thickness and woven from carbon fibers, on the one side of which the catalyst layer is deposited. The carbon cloth is treated with 40–70 wt.% poly-tetrafluoroethylene (PTFE, e.g., Teflon®) mixed with 10–20 nm carbon particles followed by sintering to melt the PTFE and coat the carbon fibers [42] and rendering it quite hydrophobic. The initial porosity of the carbon cloth is 70–80%, but its finished porosity is 55–65%.

The catalyst layer is 5–50 μm in thickness and contains Pt microcrystallites, roughly 2–4 nm in diameter, supported on the surface of largely non-porous carbon black particles, around 30 nm in diameter, at a Pt/C loading of about 20–40 wt.% and $\leq 0.4\,\mathrm{mg\,Pt/cm^2}$ of MEA area. The interstitial spaces among the carbon particles are filled with an ionomer (e.g., Nafion®) solution to allow proton transport [48], and occasionally with some PTFE, although the latter may not be necessary for thin catalyst layers [60]. The deposition of the catalyst layer on the gas-diffusion electrode is accomplished by painting, spraying, or filtration, of the catalyst/ionomer dispersion. A polymer electrolyte membrane (e.g., Nafion® 115 or 117), 50–175 μm thick, is hot-pressed at a temperature slightly above its glass transition temperature between the two electrodes such that the catalyst layers are on either side of the membrane. Alternate fabrication procedures are also employed [60].

The electrons produced at the anode catalyst surface are conducted via the carbon catalyst support and the carbon fibers of the gas-diffusion backing to the current collector and thence to the external circuit. The protons diffuse through the ionomer solution within the catalyst layer and then through the PEM to arrive at the cathode. The catalyst layer is, thus, designed to maximize the interfacial area among the its various phases, namely, the catalyst crystallites, the carbon support, the hydrophilic region consisting of ionomer, and any hydrophobic region containing Teflon®.

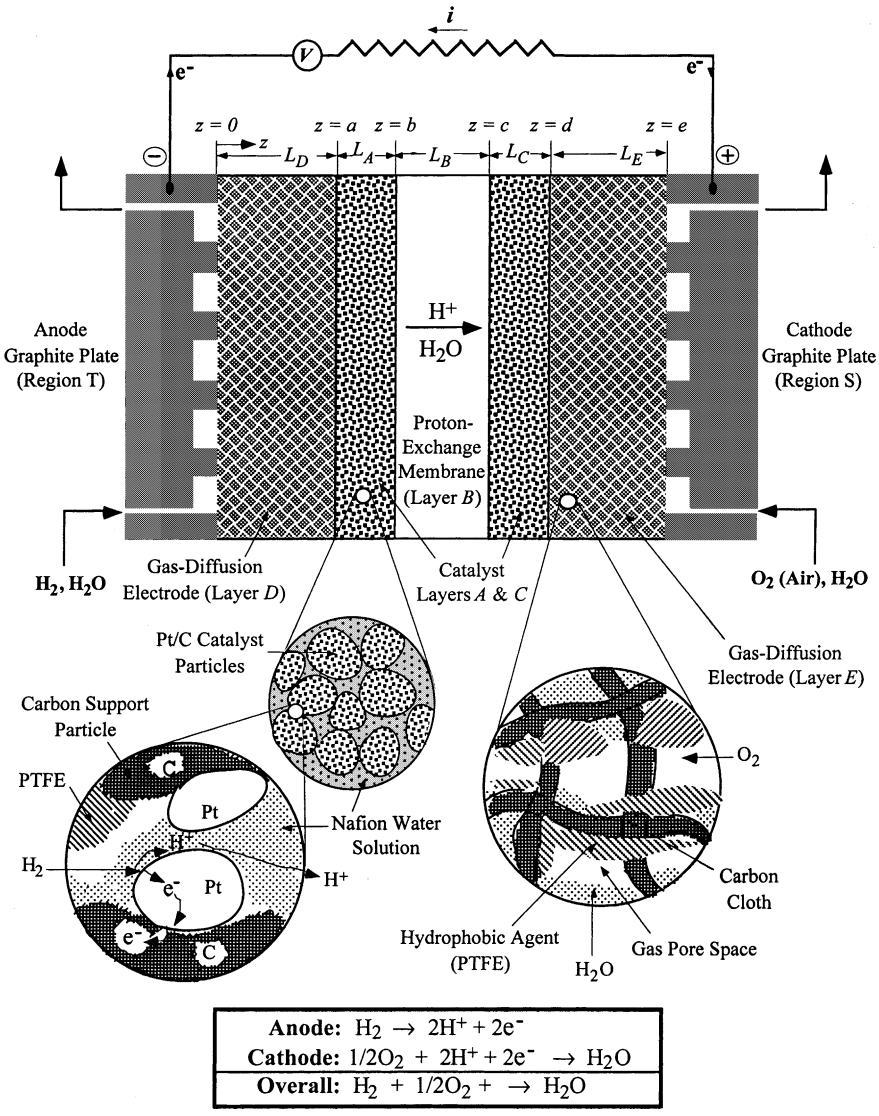

Fig. 1. A schematic representation of the PEM fuel cell cross-section consisting of gas-diffusion backing (layers D and E), catalyst layers (layers A and C), and the PEM (layer B). The gas-diffusion backing fibers are coated with PTFE so as to be not flooded with water, while the catalyst layers comprise ionomer solution among Pt/C particles for proton transport.

In addition to good interfacial contact among the layers, the continuity of the respective phases for electronic and protonic conduction is also essential. If there is too little ionomer, for instance, the proton conduction pathway will be fragmented. On the other hand, too much ionomer could compromise electronic conductivity by further distancing the carbon particles and increasing the path length for proton conduction.

The PFSA membranes such as Nafion® produced by Du Pont (and similar membranes produced by Dow, W.L. Gore, and Asahi Glass) consist of a fluorocarbon, Teflon®-like, backbone with side-chains culminating in $-SO_3H$ groups. In the presence of water, these sulfonic acid groups dissociate, forming hydronium ions [28] responsible for proton conduction. There are many studies on the nanostructural aspects of the

Nafion® membranes. Based on small angle X-ray diffraction and other characterization studies, Gierke and co-workers [21,22] proposed in their "cluster-network model" that the incompatibility of the fluorocarbon and the hydrophilic phase leads to the formation of inverted micelles, 3–5 nm in diameter, which are interconnected through short narrow channels, 1–2 nm in diameter, to provide a network for proton diffusion interspersed throughout the fluorocarbon matrix. The conductivity of Nafion® is extremely sensitive to relative humidity (RH), being essentially an insulator below a threshold of about 10% RH and rising through several orders of magnitude to about 0.07 S/cm at 80°C and 100% RH [56]. The mechanism involving ordinary diffusion and Grotthus chain conduction explaining high proton conductivity in aqueous solutions is discussed by Glasstone et al. [23] and Bockris and Reddy [8]. Nafion® also deters short-circuiting of electrons, as well as cross-over of reactants, its permeability of H_2 and O_2 being of the order of only 10^{-10} mol/cm^2 s atm [27].

3. Constitutive relations

The mass balance equations for species i $(i = 1, 2, \ldots, n)$

$$\nabla \cdot \boldsymbol{N}_i = \sum_{\rho=1}^{q} i_\rho r_\rho \tag{1}$$

need to be solved subject to appropriate boundary conditions in the various layers of the fuel cell MEA (Fig. 1), for which flux relations for the different layers are needed as well as the kinetics of the anode and cathode reactions. Since the constitutive relations used here are somewhat different from those used conventionally, these are first discussed. Once the species fluxes are determined, the current density is obtained from

$$\boldsymbol{i} = F \sum_{i=1}^{n} z_i \boldsymbol{N}_i \tag{2}$$

3.1. Dusty-fluid model

The flux model for $\boldsymbol{N}_i$ in a porous layer α is assumed here to be the dusty-fluid model (DFM) [38], written in the form [56]

$$-\frac{c_i}{RT}\nabla_{\mathrm{T}}\mu_i^{\mathrm{e}} = \sum_{\substack{j=1\\ j\neq i}}^{n} \frac{1}{cD_{ij}^{\mathrm{e}}}(c_j\boldsymbol{N}_i - c_i\boldsymbol{N}_j) + \frac{\boldsymbol{N}_i}{D_{i\mathrm{M}}^{\mathrm{e}}} + \frac{c_i B_0}{\mu D_{i\mathrm{M}}^{\mathrm{e}}} \times \left[\nabla p + \left(\sum_{j=1}^{n} c_j z_j\right) F\nabla\phi\right] \quad (i = 1, 2, \ldots, n) \tag{3}$$

where the electrochemical potential gradient on the left-hand side represents the driving force for an electrochemical system, $\nabla_{\mathrm{T}}\mu_i^{\mathrm{e}} = \nabla_{\mathrm{T}}\mu_i + z_i F\nabla\phi$. The DFM includes ordinary diffusion represented by D_{ij}^{e}, membrane diffusion represented by $D_{i\mathrm{M}}^{\mathrm{e}}$ that accounts for the friction between i and the membrane, as well as convective flux represented by the last term on the right-hand side (rhs) of Eq. (3), which includes contributions both due to a pressure gradient (d'Arcy term) as well as a potential gradient (electroosmosis). The d'Arcy permeability and the effective diffusion coefficients in the DFM for layer α are given by the relations

$$D_{ij}^{\mathrm{e}} = K_{1\alpha}D_{ij} = (\varepsilon_\alpha - \varepsilon_{\alpha 0})^q D_{ij}, \quad D_{i\mathrm{M}}^{\mathrm{e}} = K_{0\alpha}D_{i\mathrm{M}}, \quad B_{0\alpha} = \tfrac{1}{8}(\varepsilon_\alpha - \varepsilon_{\alpha 0})^q a_\alpha^2 \tag{4}$$

where ε_α is the void fraction of layer α, $\varepsilon_{\alpha 0}$ is the corresponding percolation threshold, and the critical (or Bruggeman) exponent $q = 1.5$ [56] and a_α is the mean pore radius. Summing Eq. (3) over all species, the Stefan–Maxwell terms cancel out, resulting in

$$\left[\nabla p + \left(\sum_{j=1}^{n} c_j z_j\right) F\nabla\Phi\right] = -\frac{RT}{W}\sum_{j=1}^{n}\frac{\boldsymbol{N}_j}{D_{j\mathrm{M}}^{\mathrm{e}}} \tag{5}$$

where

$$W \equiv 1 + \frac{B_0 cRT}{\mu}\sum_{h=1}^{n}\frac{x_h}{D_{h\mathrm{M}}^{\mathrm{e}}} \tag{6}$$

Using Eq. (5) into Eq. (3) to eliminate the convective driving force on its rhs, the DFM may be written in the following alternate form

$$-\frac{c_i}{RT}\nabla_T\mu_i^{\mathrm{e}} = \sum_{\substack{j=1\\ j\neq i}}^{n}\frac{1}{cD_{ij}^{\mathrm{e}}}(c_j\boldsymbol{N}_i - c_i\boldsymbol{N}_j) + \frac{\boldsymbol{N}_i}{D_{i\mathrm{M}}^{\mathrm{e}}} - \frac{c_i B_0 RT}{\mu D_{i\mathrm{M}}^{\mathrm{e}} W}\sum_{j=1}^{n}\frac{\boldsymbol{N}_j}{D_{j\mathrm{M}}^{\mathrm{e}}} \quad (i = 1, 2, \ldots, n) \tag{7}$$

This form of DFM contains the driving force for i on the left-hand side, and fluxes of all species on the rhs. It may, of course, be inverted to alternately provide flux of species i in terms of the driving forces of all species [56]. However, if the flux ratios N_j/N_i of the various species j with respect to the key species i are known, as, e.g., through reaction stoichiometry (as in the case for fuel cells), the following Fickian form for flux may be obtained

$$N_i = -\frac{1}{RT} D_i^{\mathrm{e}} c_i \nabla_{\mathrm{T}} \mu_i^{\mathrm{e}} \quad (i = 1, 2, \ldots, n) \tag{8}$$

where the effective diffusivity is

$$\frac{1}{D_i^{\mathrm{e}}} = \sum_{\substack{j=1 \\ j\neq i}}^{n} \frac{1}{cD_{ij}^{\mathrm{e}}} \left(c_j - c_i \frac{N_j}{N_i} \right) + \frac{1}{D_{i\mathrm{M}}^{\mathrm{e}}} - \frac{c_i B_0 RT}{\mu D_{i\mathrm{M}}^{\mathrm{e}} W} \sum_{j=1}^{n} \frac{1}{D_{j\mathrm{M}}^{\mathrm{e}}} \frac{N_j}{N_i} \quad (i = 1, 2, \ldots, n) \tag{9}$$

These results are used to obtain permeability of the gas-diffusion layers as well as the conductivity of the PEM.

3.2. Transport of gases in gas-diffusion backing (layers D and E)

Although it has been conventional to use Stefan–Maxwell equations to describe the gas-phase diffusion in GDB [5,50,53,59], these equations include only the molecular diffusion and are, in general, incomplete for description of transport of gases in porous media. Thus, the dusty-gas model (DGM) [29,38], obtained simply from the DFM described above specialized to the case of gases is utilized here. For the case of gaseous transport, the driving force in DFM reduces simply to $c_i \nabla_{\mathrm{T}} \mu_i^{\mathrm{e}} = \nabla p_i$. Further, the membrane diffusion coefficient $D_{i\mathrm{M}}^{\mathrm{e}}$ simply becomes the familiar Knudsen diffusion $D_{i\mathrm{K}}^{\mathrm{e}}$ coefficient for gases.

Actually, the effective diffusivity in a partially liquid-filled porous layer α is appropriately given by [13]

$$D_{i\alpha}^{\mathrm{e}} = (1 - q_{\mathrm{w}})^q D_{i\mathrm{G}}^{\mathrm{e}} + q_{\mathrm{w}}^q \kappa_{i\mathrm{L}} K_1 D_{i\mathrm{L}} \approx (1 - q_{\mathrm{w}})^q D_{i\mathrm{G}}^{\mathrm{e}} \tag{10}$$

where $D_{i\mathrm{L}}$ is the liquid-phase diffusivity, and $D_{i\mathrm{G}}^{\mathrm{e}}$ is the effective gas-phase diffusivity for the *dry* porous layer. Eq. (10) accounts for the simultaneous transport of species i through the residual gas pore space as well as any through the liquid phase. The approximation on the rhs of Eq. (10) is made here, however, assuming that the flux contribution of the aqueous phase within the gas-diffusion layers is unimportant due to the low solubility (small partition coefficient, $\kappa_{i\mathrm{L}}$) of the gases. The gas-phase diffusivity in Eq. (10) is obtained from Eq. (9), written in terms of partial pressures, however, rather than concentrations

$$\frac{1}{D_{i\mathrm{G}}^{\mathrm{e}}} = \frac{1}{D_{i\mathrm{K}}^{\mathrm{e}}} + \sum_{\substack{j=1 \\ j\neq i}}^{n} \frac{1}{D_{ij}^{\mathrm{e}0}} \left(p_j - p_i \frac{N_j}{N_i} \right) - \frac{p_i B_0}{\mu W D_{i\mathrm{K}}^{\mathrm{e}}} \sum_{j=1}^{n} \frac{N_j}{N_i} \frac{1}{D_{j\mathrm{K}}^{\mathrm{e}}} \tag{11}$$

Here the pressure-independent ordinary diffusivity and the effective Knudsen diffusivity [29]

$$D_{ij}^{\mathrm{e}0} \equiv p D_{ij}^{\mathrm{e}} = p K_1 D_{ij}, \qquad D_{i\mathrm{K}}^{\mathrm{e}} = K_0 \sqrt{\frac{8RT}{\pi M_i}} \tag{12}$$

where the dusty-gas structural parameters for the dry porous layer for Knudsen diffusion is $K_0 = (\varepsilon_\alpha - \varepsilon_{\alpha 0})^q (\frac{1}{3} 2 a_\alpha)$.

As done by others (e.g., [5]), it is next assumed that due to the presence of liquid water in the pores of the gas-diffusion backing, the gas phase is saturated with water vapor, i.e., the partial pressure of water is equal to its vapor pressure at the fuel cell temperature ($p_{\mathrm{w}} = p_{\mathrm{w}}^0$). Thus, under isothermal conditions, there is no partial pressure gradient of water vapor in GDB. Although this does not necessarily imply that the water vapor flux in the gas phase is zero, for simplicity it is further assumed here that $N_{\mathrm{w}} = 0$. In other words, water transport is assumed to occur entirely through the liquid phase. Further, for N_2 in the case of cathode and CO_2 in the case of anode, denoted as the diluent species d, $N_{\mathrm{d}} = 0$. Using this in Eqs. (6) and (11), the effective diffusivity of i (H_2 in the case of anode, or O_2 in the case of cathode)

$$\frac{1}{D_{i\mathrm{G}}^{\mathrm{e}}} = \frac{p_{\mathrm{w}}}{D_{i\mathrm{w}}^{\mathrm{e}0}} + \frac{p_{\mathrm{d}}}{D_{i\mathrm{d}}^{\mathrm{e}0}} + \frac{1}{D_{i\mathrm{K}}^{\mathrm{e}}} \times \left\{ \frac{1 + (B_0/\mu)((p_{\mathrm{w}}/D_{\mathrm{wK}}^{\mathrm{e}}) + (p_{\mathrm{d}}/D_{\mathrm{dK}}^{\mathrm{e}}))}{1 + (B_0/\mu)((p_i/D_{i\mathrm{K}}^{\mathrm{e}}) + (p_{\mathrm{w}}/D_{\mathrm{wK}}^{\mathrm{e}}) + (p_{\mathrm{d}}/D_{\mathrm{dK}}^{\mathrm{e}}))} \right\} \tag{13}$$

3.3. Transport of protons in PEM (layer B)

We have recently shown [56] that for binary case of proton transport in a PEM consisting of water as the solvent (species w), and the hydronium ion (H_3O^+), denoted as species H^+, as the charge carrier, and for spatially homogeneous sulfonic acid groups within PEM coupled with local electroneutrality, the electrochemical potential gradient simply becomes potential gradient. Further, for equimolar counter-diffusion and for $D^{e}_{H^+M} \approx D^{e}_{wM}$ due to the similarity between w (water) and H^+ (hydronium ion), the effective diffusivity (Eq. (9)) reduces to

$$\frac{1}{D^{e}_{H^+}} \approx \frac{1}{D^{e}_{H^+w}} + \frac{1}{D^{e}_{H^+M}} \tag{14}$$

namely, the Bosanquet equation ([29, p. 36]). Further, with $\sigma = (F^2/RT) D^{e}_{H^+} c_{H^+}$, and $c_{H^+} = c_{HA,0}\alpha$, and in terms of the equivalent conductance, $\lambda^0_{H^+} \equiv F^2 |z_{H^+}| D_{H^+w}/RT$, the conductivity of PEM becomes

$$\sigma = (\varepsilon_B - \varepsilon_{B0})^q \left(\frac{\lambda^0_{H^+,298}}{1+\delta}\right) \times \exp\left\{-\frac{E_\mu}{R}\left(\frac{1}{T} - \frac{1}{298}\right)\right\} c_{HA,0}\alpha \tag{15}$$

where the ratio $\delta \equiv D^{e}_{H^+w}/D^{e}_{H^+M}$, and the degree of dissociation in terms of the equilibrium constant $K_{A,C}$ for the protonation reaction, $AH + H_2O \leftrightarrows H_3O^+ + A^-$, is

$$\alpha = \frac{(\lambda+1) - \sqrt{(\lambda+1)^2 - 4\lambda(1 - 1/K_{A,C})}}{2(1 - 1/K_{A,C})} \tag{16}$$

where

$$K_{A,C} = K_{A,C,298} \exp\left[-\frac{\Delta H^0}{R}\left(\frac{1}{T} - \frac{1}{298}\right)\right] \tag{17}$$

The volume fraction of water in PEM is related to the number of water molecules sorbed per $–SO_3H$ group, λ,

$$\varepsilon_B = \frac{\lambda}{(\bar{V}_M/\bar{V}_w) + \lambda} \tag{18}$$

where $\bar{V}_M \approx EW/\rho_0 = 537\,cm^3/mol$, and $\bar{V}_w = 18\,cm^3/mol$. The water molecules sorbed are given in terms of relative humidity (RH, or a_w), by n_w-layer Brunauer–Emmett–Teller (BET) equation [2]

$$\frac{\lambda}{\lambda_m} = \frac{[Ca_w/(1-a_w)][1 - (n_w+1)a_w^{n_w} + n_w a_w^{n_w+1}]}{1 + (C-1)a_w - Ca_w^{n_w+1}} \tag{19}$$

where the RH or the water vapor activity, $a_w = p_w/p^0_w$, λ_m is the water loading at monolayer coverage, and n_w is the total number of water layers in the pores at saturation. We have recently shown that the above model for proton conduction in PEM provides an excellent correlation with a variety of experimental data [56].

3.4. Electrocatalysis: general considerations

Some of the general characteristics of electrocatalytic reactions are first presented, including how their rates are influenced by potential. Consider the electrode surface reaction ρ

$$\sum_{\substack{i=1 \\ i\neq e^-}}^{n} \nu_{\rho i} A_i^{z_i} + \nu_{\rho e^-} e^- = 0 \tag{20}$$

among n species, $A_i^{z_i}$, carrying a charge z_i, where $\nu_{\rho e^-}$ is the stoichiometric coefficient of the electron in reaction ρ. Thus, $\nu_{\rho e^-} = +n_\rho$ for an anodic reaction while $\nu_{\rho e^-} = -n_\rho$ for a cathodic reaction, where n_ρ is the number of electrons involved in the reaction ρ. There is, of course, overall charge balance in the electrode reaction, i.e.,

$$\sum_{\substack{i=1 \\ i\neq e^-}}^{n} \nu_{\rho i} z_i = \nu_{\rho e^-} \tag{21}$$

For an *elementary* electrode reaction ρ, the net rate of reaction per unit supported metal catalyst surface area, r^*_ρ (e.g., mol/cm^2 Pt s), from the thermodynamic formulation of the transition-state theory (TTST) [10] is

$$r^*_\rho = \vec{r}^*_\rho - \overleftarrow{r}^*_\rho = \vec{k}^*_\rho \prod_{i=1}^{r} a_i^{-\nu_{\rho i}} - \overleftarrow{k}^*_\rho \prod_{i=r+1}^{n} a_i^{\nu_{\rho i}} \tag{22}$$

where the first r of the total of n species are assumed to be the reactants while the remaining are products.

For surface species, the activity in Eq. (22) corresponds to surface activity, which for an ideal surface is just the fractional surface coverage. The potential dependence of the rate constants

$$\vec{k}^*_\rho = \vec{k}^*_{\rho,\Phi_0} \exp\left\{\frac{\beta_\rho \nu_{\rho e^-} F\eta}{RT}\right\},$$
$$\overleftarrow{k}^*_\rho = \overleftarrow{k}^*_{\rho,\Phi_0} \exp\left\{\frac{(\beta_\rho - 1)\nu_{\rho e^-} F\eta}{RT}\right\} \quad (23)$$

where $\vec{k}^*_{\rho,\Phi_0}$ is the rate constant at the equilibrium electrode potential Φ_0, i.e.,

$$\vec{k}^*_{\rho,\Phi_0} = \left(\kappa \frac{k_B T}{h\gamma^\pm} e^{(\Delta \vec{S}^{\pm 0}_{\rho T,\Phi=0}/R)}\right) \times \exp\left(-\frac{\Delta \vec{H}^{\pm 0}_{\rho T,\Phi=0} - \beta_\rho \nu_{\rho e^-} F\Phi_0}{RT}\right) \equiv A_\rho \exp\left(-\frac{E_{\rho,\Phi_0}}{RT}\right) \quad (24)$$

and similarly for $\overleftarrow{k}_{\rho,\Phi_0}$. These equations clearly show that the potential has a powerful effect on the Gibbs free energy of activation and hence the rate constants of electrodic reactions, in addition, of course, to the strong effect of temperature. In the above, Φ_0 is a function of composition as given by the Nernst equation, $\eta \equiv \Phi - \Phi_0$ is the electrode overpotential, and β_ρ is the so-called symmetry factor for the reaction ρ, also referred to as the transfer coefficient resulting from the application of linear free energy relationship, universally assumed to be one-half for elementary reactions [10]. The second form of the rate constant Φ_0 in Eq. (24) is the usual Arrhenius form, for which the pre-exponential factor and activation energy may be obtained by comparison with the TTST form. It may be noted that the effect of potential on the forward and reverse rate constants is such that one increases while the other reduces with overpotential. The ratio, $K_\rho = \vec{k}_\rho / \overleftarrow{k}_\rho$, namely the equilibrium constant for the elementary reaction ρ

$$K_\rho = K_{\rho,\Phi_0} \exp\left(\frac{\nu_{\rho e^-} F\eta}{RT}\right) \quad (25)$$

is also greatly influenced by potential.

Under open-circuit conditions for the given composition, $\eta = 0$, $r^*_\rho = 0$, and, thus, from Eqs. (22) and (23)

$$\vec{r}^*_{\rho 0} = \vec{k}^*_{\rho,\Phi_0} \prod_{i=1}^{r} a_i^{-\nu_{\rho i}} = \overleftarrow{r}^*_{\rho 0} = \overleftarrow{k}^*_{\rho,\Phi_0} \prod_{i=r+1}^{n} a_i^{\nu_{\rho i}} \quad (26)$$

i.e., the cell potential assumes the equilibrium value Φ_0, corresponding to the given composition and temperature, so that the forward and reverse reactions rates are equal and a dynamic equilibrium is established. This may be rearranged into the well-known Nernst equation,

$$\Phi_0 = \Phi_0^0 + \frac{RT}{F\nu_{\rho e^-}} \ln \prod_{\substack{i=1 \\ i \neq e^-}}^{n} a_i^{\nu_\rho i} \quad (27)$$

where Φ_0^0 is the standard equilibrium electrode potential corresponding to unit species activities.

The above kinetic equations may be written in the form of the Butler–Volmer equation as follows. Using Eqs. (23) and (26), Eq. (22) may be written as

$$r^*_\rho = \vec{r}^*_{\rho 0}\left[\exp\left\{\frac{\beta_\rho \nu_{\rho e^-} F\eta}{RT}\right\} - \exp\left\{\frac{(\beta_\rho - 1)\nu_{\rho e^-} F\eta}{RT}\right\}\right] = \overleftarrow{r}^*_{\rho 0}\left[\exp\left\{\frac{\beta_\rho \nu_{\rho e^-} F\eta}{RT}\right\} - \exp\left\{\frac{(\beta_\rho - 1)\nu_{\rho e^-} F\eta}{RT}\right\}\right] \quad (28)$$

or in a pseudo-irreversible form

$$r^*_\rho = k^*_\rho \prod_{i=1}^{r} a_i^{-\nu_{\rho i}} \quad (29)$$

where the effective rate constant is given by the Butler–Volmer form

$$k^*_\rho = \vec{k}^*_{\rho,\Phi_0}\left\{\exp\left(\frac{\beta_\rho \nu_{\rho e^-} F\eta}{RT}\right) - \exp\left(\frac{(\beta_\rho - 1)\nu_{\rho e^-} F\eta}{RT}\right)\right\} \quad (30)$$

For the common value $\beta_\rho = \frac{1}{2}$, this may be written in the more convenient alternate form

$$k^*_\rho = \vec{k}^*_{\rho,\Phi_0}\left\{2\sinh\left(\frac{\nu_{\rho e^-} F\eta}{2RT}\right)\right\} \quad (31)$$

The corresponding current density of i^* (A/cm^2 catalyst surface) is obtained from

$$i^* = F\sum_{\substack{i=1\\ i\neq e^-}}^{n} z_i N_i^* = F r_\rho^* \sum_{\substack{i=1\\ i\neq e^-}}^{n} z_i \nu_{\rho i} = F \nu_{\rho e^-} r_\rho^* \qquad (32)$$

where the current direction is determined by the stoichiometric coefficient of electrons. The second equality in Eq. (32) stems from the assumption of the absence of diffusional limitations, while the third equality utilizes Eq. (21). Similarly, the exchange-current density, namely the current in the forward and reverse direction under open circuit conditions, $i_0^* = F\nu_{\rho e^-}\vec{r}_{\rho 0}^*$, which depends upon temperature and composition.

The current density i in terms of A/cm^2 of geometric (MEA) area is $i = \gamma_M i^*$ and $i_0 = \gamma_M i_0^*$. Here, the ratio of electrochemically active metal catalyst surface area to the geometric MEA area (cm^2 Pt/cm^2 geometric MEA area) [24], also frequently referred to as the roughness factor [40]

$$\gamma_M = \varphi_I m_M \left(\frac{6\varphi_M}{\rho_M d_M}\right) \qquad (33)$$

where φ_M accounts for the part of the metal crystallite of diameter d_M which is not accessible for reaction, e.g., the side which is in contact with the support, and φ_I is the fraction of the available metal surface participating in electrocatalysis. This would be less than unity, e.g., if not all of the available metal area is in contact with the ionomer, and hence depends upon ionomer loading m_I. Using the above, the current density is related to exchange-current density and over-potential by

$$\frac{i^*}{i_0^*} = \frac{i}{i_0} = \left\{2\sinh\left(\frac{\nu_{\rho e^-} F\eta}{2RT}\right)\right\} \qquad (34)$$

For large overpotential η, this reduces to the familiar Tafel equation

$$\frac{i}{i_0} \approx \exp\left(\frac{\nu_{\rho e^-} F\eta}{2RT}\right) \qquad (35)$$

whereas for small overpotential η, may be approximated by a linear form

$$\frac{i}{i_0} \approx \frac{\nu_{\rho e^-} F\eta}{RT} \qquad (36)$$

3.5. Hydrogen oxidation reaction (HOR)

The catalytic hydrogen electrode reaction

$$H_2 \leftrightarrows 2H^+ + 2e^- \qquad (37)$$

has been much studied [11], but its mechanism and kinetics are still uncertain [17,36]. The two most common mechanisms are the so-called Tafel–Volmer mechanism and the Heyrovsky–Volmer mechanism [17]. The former constitutes a Tafel step, namely, the dissociative chemisorption of hydrogen, which is usually assumed to be the rate-determining step (rds), followed by a Volmer step involving dissociation of the adsorbed hydrogen atom to produce an electron and a solvated proton, i.e.,

$$\text{Tafel step}: \quad 2S + H_2 \leftrightarrows 2S\cdot H \quad \text{(rds)} \qquad (38)$$

$$\text{Volmer step}: \quad S\cdot H \leftrightarrows S + H^+ + e^- \qquad (39)$$

where S represents a catalyst site. A rate expression for the HOR is [19]

$$r_A^* = \vec{k}_A^* c_{H_2} \exp\left(\frac{\vec{\alpha}_A F\eta_A}{RT}\right) - \overleftarrow{k}_A^* c_{H^+}^2 \exp\left(-\frac{\overleftarrow{\alpha}_A F\eta_A}{RT}\right) \qquad (40)$$

The lack of an adsorption term in the denominator of this expression may be justified in view of $\theta_{S\cdot H} \ll 1$. Following the development in the above section, for the effective transfer coefficient of the overall HOR, $\vec{\alpha}_A = \overleftarrow{\alpha}_A = \frac{1}{2}$, this may be written in the pseudo-irreversible form

$$r_A^* = k_A^* c_{H_2} \qquad (41)$$

where

$$k_A^* = \vec{k}_{A,\Phi_0}^* \left\{2\sinh\left(\frac{\vec{\alpha}_A F\eta_A}{RT}\right)\right\} \qquad (42)$$

Further, from $i_{A,0}^* = F\nu_{Ae^-}\vec{r}_{A0}^*$ with $\nu_{Ae^-} = +2$ (reaction 37), the *reference* exchange current density, $i_{A,0,ref}^* = 2F\vec{k}_{A,\Phi_0}(T_{ref})c_{H_2,ref}$. The reaction is very rapid, particularly as compared with the oxygen reduction reaction at the cathode, with an exchange current density $i_{A,0,ref}^* \approx 1$ mA/cm^2 Pt (e.g., [27]) at standard conditions, so that the overpotential due to the HOR is relatively small. Even though the HOR is very facile on Pt, the many species emanating from the reformer

can successfully compete with it for Pt sites. In particular, for reformed hydrocarbons, anode feed may contain roughly 100 ppm CO, which adsorbs on Pt

$$S + CO \leftrightarrows CO \cdot S \tag{43}$$

Since the adsorption enthalpy of CO on Pt (−32 kcal/mol) is much higher than that for the other species present, it may be considered as the most abundant surface species [9]. For instance, at 100 ppm, roughly 90% of the sites are occupied by CO. Under such conditions, therefore, the rate of HOR must be modified to include $(1 - \theta_{CO\cdot S})^2$ on its rhs [58]. Thus, with $i_{A,0} = \gamma_{MA} i^*_{A,0}$, the exchange-current density

$$i_{A,0} = \gamma_{M,A}(1 - \theta_{CO\cdot S})^2 \left(\frac{c_{H_2}}{c_{H_2,ref}}\right) \exp\left\{-\frac{E_{A,\Phi_0}}{R}\left(\frac{1}{T} - \frac{1}{T_{ref}}\right)\right\} i^*_{A,0,ref} \tag{44}$$

where E_{A,Φ_0} is the effective activation energy of $i_{A,0}$ or $\vec{k}_{A,\Phi_0}$ (Eq. (24)). Thus, increasing $i_{A,0}$ may be accomplished by increasing $\gamma_{M,A}$, temperature, and H_2 concentration and reducing poisoning.

3.6. Oxygen reduction reaction

The catalytic oxygen reduction reaction (ORR)

$$O_2 + 4H^+ + 4e^- \leftrightarrows 2H_2O \tag{45}$$

has also been extensively investigated due to its great importance in energy conversion and storage, and a large number of mechanisms have been proposed [33,36], none of which are entirely satisfactory from the viewpoint of observed kinetics. Certain experimental features of the reaction under acidic conditions, however, are well established [52]: (i) two different Tafel slopes are observed, namely around −60 mV ($-2.303\,RT/F$) at low cds (3×10^{-7} to about 3×10^{-5} A cm^{-2}) and −120 mV ($-2.303\,2RT/F$) at higher cds ($> 3 \times 10^{-5}$ A cm^{-2}); (ii) reduction is first-order in oxygen at all cds; (iii) it is 1.5 order in proton concentration at low cds and first-order at higher cds [12]; (iv) the surface coverage of adsorbed oxygen is probably small [12]; and (v) H_2O_2 is a detectable intermediate. We adopt the following rate expression [51]

$$r^*_C = k^*_C c_{O_2} c_{H^+} \tag{46}$$

with

$$k^*_C = \vec{k}^*_{C,\Phi_0}\left\{2\sinh\left(-\frac{\vec{\alpha}_C F \eta_C}{RT}\right)\right\} \tag{47}$$

As mentioned above, the effective transfer coefficient $\vec{\alpha}_C = 1$ (Tafel slope, $b = 2.303\,RT/F$) at low cds (fuel cell voltages above 0.8 V), while below this voltage (high cds), frequently $\vec{\alpha}_C = \frac{1}{2}$ (Tafel slope, $b = 2.303 \times 2RT/F$) is observed [45,52]. Since most of the overpotential occurs at low cds, in this analysis we assume $\vec{\alpha}_C = 1$ at all cds. A more accurate analysis might utilize two different effective transfer coefficients. On the other hand, this doubling of slope may also been explained simply on the basis of diffusional control at higher cds [33]. The exchange current density under reference conditions from $i^*_{C,0} = F\nu_{Ce^-}\vec{r}^*_{C0}$, with $\nu_{Ce^-} = -4$, is $i^*_{C,0,ref} = -4(c^*_t/c^2)\vec{k}_{1C,\Phi_0}(T_{ref})c_{O_2,ref}c_{H^+,ref}$. Thus

$$i_{C,0} = \gamma_{M,C}\left(\frac{c_{O_2}}{c_{O_2,ref}}\right)\left(\frac{c_{H^+}}{c_{H^+,ref}}\right) \times \exp\left\{-\frac{E_{C,\Phi_0}}{R}\left(\frac{1}{T} - \frac{1}{T_{ref}}\right)\right\} i^*_{C,0,ref} \tag{48}$$

4. MEA analysis

In order to analyze the fuel cell as a membrane reactor, the following steady-state one-dimensional conservation equations are considered in the MEA [14,31]:

Anode Chamber (Region T)

$$F_T(c_{iT,0} - c_{iT}) = N_{iz}(0) \cdot A \tag{49}$$

GDB (Layers D and E)

$$\frac{dN_{iz}}{dz} = 0, \qquad N_{iz} = -D^e_{i\alpha}\frac{dc_i}{dz} \tag{50}$$

PEM (Layer B)

$$\frac{di}{dz} = 0, \qquad i = -\sigma\frac{d\phi}{dz} \tag{51}$$

Catalyst (Layers A and C)

$$\frac{dN_{iz}}{dz} = \nu_{\rho i} r_\rho, \quad N_{iz} = -\frac{1}{RT}D^e_{i\alpha}\left(\frac{dc_i}{dz} + z_i c_i F\frac{d\phi}{dz}\right) \tag{52}$$

Cathode Chamber (Region S)

$$F_S(c_{iS,0} - c_{iS}) = N_{iz}(e) \cdot A \tag{53}$$

The anode and the cathode chamber equations are for a single (differential) fuel cell rather than for a stack. For our purpose here, it is assumed that both pure hydrogen and oxygen are fed into the anode and cathode chambers, so that in $c_{iT} = c_{iT,0}$ and $c_{iS} = c_{iS,0}$, although this would not hold if reformate and air were used. Further, while as discussed above, the effective diffusivities in the GDBs are clearly functions of composition and hence position, they are assumed to be constant here in order to obtain an analytical solution. The solution for flux in the gas-diffusion layer α (layer D or E) obtained by integrating Fickian flux equation for constant flux and constant effective diffusivity is

$$N_{i\alpha} = P_{i\alpha}\left\{c_{iG} - \frac{c_{i\alpha}(L_\alpha)}{\kappa_{i\alpha}}\right\} \tag{54}$$

In this, the permeability of species i is $P_{i\alpha} \equiv \kappa_{i\alpha} D_{i\alpha}/L_\alpha$, where $\kappa_{i\alpha} \equiv (c_{i\alpha}/c_{iG})_{eq}$ is the partition coefficient for phase α.

For the PEM similarly for constant conductivity, the solution is

$$i = \frac{\sigma}{L_B}\{\phi_{S,B}(b) - \phi_{S,B}(c)\} \tag{55}$$

In order to obtain a simple analytical solution, we shall assume that the catalyst layers are thin enough so that (i) there is no potential drop and further, (ii) there are no diffusional limitations within these layers. While there is some support for the former through the numerical calculations of Bernardi and Verbrugge [5], the latter assumption is likely to be erroneous at higher cds. Nonetheless, the rate of the anodic reaction within the catalyst layer under these assumptions can be written as $r_A^* = k_A^* c_{H_2,A}(a)$ from Eq. (41) along with $c_{H_2,A} = c_{H_2,A}(a)$, i.e., the concentration of hydrogen throughout the catalyst layer is assumed to be uniform and equal to its value at $z = a$ (Fig. 1). Using this in $i_A^* = F\nu_{Ae^-} r_A^*$ along with $i_A = \gamma_M i_A^*$ gives the anode current density

$$i_A = \gamma_{MA} F \nu_{Ae^-} k_A^* c_{H_2,A}(a) \tag{56}$$

where the rate constant for the anode layer is given by Eq. (42) while γ_{MA} is given by Eq. (33). Similarly, the anode exchange-current density is

$$i_{A,0} = \gamma_{MA} F \nu_{Ae^-} \vec{k}_{A,\Phi_0}^* \kappa_{H_2,A} c_{H_2,T} \tag{57}$$

where use is made of $c_{H_2,A}(a) = \kappa_{H_2,A} c_{H_2,T}$ under equilibrium conditions, since there are, of course, no diffusional limitations in the gas-diffusion backing under equilibrium conditions.

The hydrogen flux at $z = a$ for a PEM that is impervious to it is obtained from material balance

$$N_{H_2}(a) = \gamma_{MA}(-\nu_{AH_2}) k_A^* c_{H_2,A}(a) \tag{58}$$

The flux of hydrogen in the gas-diffusion backing of anode (Layer D) is obtained from Eq. (54)

$$N_{H_2}(0) = N_{H_2}(a) = P_{H_2,D}\left\{c_{H_2,T} - \frac{c_{H_2,A}(a)}{\kappa_{H_2,A}}\right\} \tag{59}$$

An expression for the anodic current density can be obtained by equating Eqs. (58) and (59), solving for $c_{H_2,A}(a)$, and then using it in Eq. (56)

$$i_A = \frac{\gamma_{MA}\nu_{Ae^-} F k_A^* \kappa_{H_2,A} c_{H_2,T}}{1 + (\gamma_{MA}(-\nu_{AH_2}) k_A^* \kappa_{H_2,A}/P_{H_2,D})} \tag{60}$$

In the case of a gas-diffusion controlled rate, neglecting unity in the denominator, Eq. (60) simplifies to provide an expression for the anodic limiting current density

$$i_{A,L} \equiv \left(\frac{\nu_{Ae^-}}{-\nu_{AH_2}}\right) F P_{H_2,D} c_{H_2,T} \tag{61}$$

Using Eqs. (57) and (61) into Eq. (60) and rearranging

$$\frac{k_A^*}{\vec{k}_{A,\Phi_0}^*} = \left\{\frac{i_A/i_{A,0}}{1 - i_A/i_{A,L}}\right\} \tag{62}$$

Finally, use of Eq. (42) into Eq. (62) results in a convenient form for the anodic overpotential

$$\eta_A = \frac{RT}{\vec{\alpha}_A F} \sinh^{-1}\left[\frac{1}{2}\left\{\frac{i_A/i_{A,0}}{1 - i_A/i_{A,L}}\right\}\right] \tag{63}$$

A similar derivation for the cathode (layer C) leads to an expression the cathodic overpotential

$$-\eta_C = \frac{RT}{\vec{\alpha}_C F} \sinh^{-1}\left[\frac{1}{2}\left\{\frac{i_C/i_{C,0}}{1 - i_C/i_{C,L}}\right\}\right] \tag{64}$$

where the cathodic limiting current

$$i_{C,L} \equiv \left(\frac{\nu_{Ce^-}}{-\nu_{C,O_2}}\right) F P_{O_2,E} c_{O_2,S} \tag{65}$$

4.1. Overall fuel cell performance

To obtain the current versus voltage relationship for the overall fuel cell we use, $V = \phi_{M,C} - \phi_{M,A} = (\Phi_{0,C} - \Phi_{0,A}) - \eta_A + \eta_C - (\phi_{S,A} - \phi_{S,C})$. Further, the potential drop in the solution phase due to the passage of current may be broken down further into individual components, i.e., $\phi_{S,A} - \phi_{S,C} = \{\phi_{S,A} - \phi_{S,B}(b)\} + \{\phi_{S,B}(b) - \phi_{S,B}(c)\} + \{\phi_{S,B}(c) - \phi_{S,C}\}$, where the first and the last terms are the interfacial resistance contributions between the two electrodes and the ion-exchange membrane, which may be substantial if poor fabrication techniques are employed or if the MEA becomes partially delaminated with use. Thus, using Eqs. (63), (64) and (57) along with $i = i_A = i_C$, in this, there results

$$V = V_0 - \frac{RT}{\vec{\alpha}_A F}\sinh^{-1}\left\{\frac{1}{2}\left(\frac{i/i_{A,0}}{1 - i/i_{A,L}}\right)\right\} - \frac{RT}{\vec{\alpha}_C F}\sinh^{-1}\left\{\frac{1}{2}\left(\frac{i/i_{C,0}}{1 - i/i_{C,L}}\right)\right\} - i\left(\frac{L_B}{\sigma_B}\right) - i(R_I) \quad (66)$$

where R_I accounts for any interfacial resistance, and the open circuit potential, $V_0 \equiv \Phi_{0,C} - \Phi_{0,A}$. The exchange current densities in Eq. (66) are given by Eqs. (44) and (48) for the anode and cathode, respectively, while the limiting current densities are given by Eqs. (61) and (65). Further, the conductivity of the PEM is given by Eq. (15). It is useful to reiterate that the key assumptions in the derivation of Eq. (66) are the neglect of potential drop and diffusional resistance within the catalyst layer. Otherwise, the model is quite complete. It is also noteworthy that for $i/i_L \to 0$, Eq. (66) reduces to a simple addition of the Butler–Volmer type terms arising from kinetics.

The power density is simply obtained from the use of $P = iV$ in Eq. (66). Thus

$$P = iV_0 - \frac{iRT}{\vec{\alpha}_A F}\sinh^{-1}\left\{\frac{1}{2}\left(\frac{i/i_{A,0}}{1 - i/i_{A,L}}\right)\right\} - \frac{iRT}{\vec{\alpha}_C F}\sinh^{-1}\left\{\frac{1}{2}\left(\frac{i/i_{C,0}}{1 - i/i_{C,L}}\right)\right\} - i^2\left(\frac{L_B}{\sigma_B}\right) - i^2(R_I) \quad (67)$$

A comparison of the theoretical model with experiments is discussed in Section 5.

5. Comparison of theory and experiments

A comparison of the theoretical model (Eq. (66)) above with PEM fuel cell experimental performance results is shown in Fig. 2 for the set of parameters listed in Table 1 and $R_I = 0$. E-TEK double-sided electrodes and Nafion® 115 membrane were used to fabricate the MEA for the fuel cell, with platinum and Nafion® loadings of $m_M = 0.4\,\text{mg Pt/cm}^2$ ($\omega_M = 0.2$ Pt on Vulcan XC 72) and $m_I = 0.7\,\text{mg/cm}^2$, respectively. The MEA was prepared by sandwiching the Nafion® membrane with electrodes on either side and placing it in a Carver hot press, Model C. The temperature of the hot-press was then raised to 130°C and a pressure of 4000 lb was applied for about 2 min. The resulting MEA was tested in a $5\,\text{cm}^2$ single cell obtained from Electrochem along with HP 6060B DC electronic load box and 6651A DC power supply to measure the polarization characteristics of the single cell. The mass flow rates of H_2 and O_2 were controlled with an FC 2900V mass flow controller (Millipore). The feed gases were bubbled through

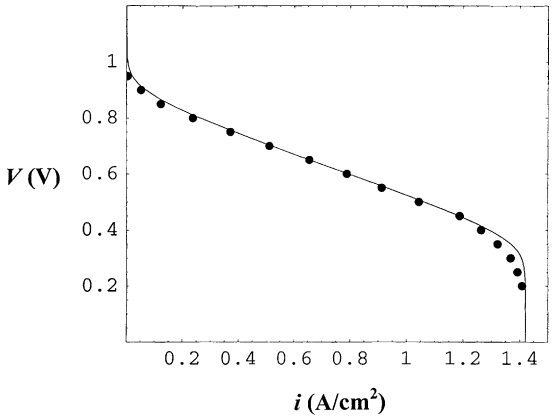

Fig. 2. Current density (A/cm^2) versus voltage (V) plot for a $5\,\text{cm}^2$ fuel cell operated at 80°C with a H_2/O_2 (30/30 psig) feed; humidifier temperatures of 95 and 90°C for anode and cathode, respectively; E-TEK double-sided electrodes with platinum catalyst ($\omega_M = 0.2$ Pt on Vulcan XC-72) loading $m_M = 0.4\,\text{mg Pt/cm}^2$ and Nafion® loading $m_I = 0.7\,\text{mg/cm}^2$, and with a Nafion® 115 membrane.

Table 1
Parameter values employed in the fuel cell model

Parameter	Value	Units/notes
PEM		
L_B	125	μm
$\bar{V}_M$	537	cm^3/mol
$\lambda^0_{H^+,298}$	349.8	S cm^2/equiv.
E_μ	14	kJ/mol
$K_{A,C,298}$	6.2	
ΔH^0	−52.3	kJ/mol
λ_0	1.9	
δ	5.5	
q	1.5	
BET parameters		
λ_m	1.8	
C	150	
n_w	13.5	
Anode/cathode catalyst		
$\vec{\alpha}_A$	$\frac{1}{2}$	
$i^*_{A,0,ref}$	10^{-3}	A/cm^2 Pt at 298 K
E_{A,Φ_0}	18	kJ/mol
$\vec{\alpha}_C$	1	
$I^*_{C,0,ref}$	10^{-11}	A/cm^2 Pt at 298 K
E_{C,Φ_0}	76	kJ/mol
ω_M	0.2	
d_M	2.9	nm
ε_{cat}	0.65	
m_M	0.4	mg/cm^2
m_I	0.7	mg/cm^2
ρ_I	0.874	g/cm^3
Gas-diffusion backing		
ε_B	0.5	
$2a$	2.1	μm
$L_D = L_E$	250	μm
κ_{H_2}	0.644	
κ_{O_2}	0.144	
q_w	0.2	

11 stainless bottles containing deionized water for the purpose of humidification. The temperature of the humidification bottles was set at 15°C and 10°C higher than the fuel cell temperature for the anode and cathode side, respectively, as commonly done.

The open circuit potential V_0 in Eq. (66) was calculated from [4]

$$V_0 = 1.23 - 0.9 \times 10^{-3}(T - 298) + \frac{RT}{4F} \ln p^2_{H_2,T} p_{O_2,S} \quad (68)$$

where T is in K, and the partial pressures are in atmospheres. The partial pressures of hydrogen and oxygen were calculated by subtracting from the total pressure the saturation pressure of water as calculated (in atm) from [49]

$$\ln p^0_w = 11.676 - \frac{3816.44}{T - 16.13} \quad (69)$$

It is apparent from Fig. 2 that the comparison between theory and experiments is very good except at very high current densities, due likely to the importance of diffusional limitations in the electrocatalyst layers at high current densities (high reaction rates) and large overpotentials. Of course, diffusional limitations in the catalyst layer have been ignored in this analysis in the interest of obtaining a simple analytical solution. Further, Fig. 3 shows a plot of the power density versus voltage for the cell along with theoretical predictions. The optimum in power density at the intermediate voltage is noteworthy and important in determining the operating voltage, which is frequently chosen to be higher than the optimum, i.e., in the range of 0.6–0.7 V. Thus, the model adequately describes the fuel cell performance except at high current densities. However, the credibility of the model clearly depends upon the reasonableness of the parameters employed, which is discussed next.

The parameters utilized in the PEM conductivity model, i.e., for the BET equation and the PEM, are those given by Thampan et al. [56], who also provide adequate justification for these values. These

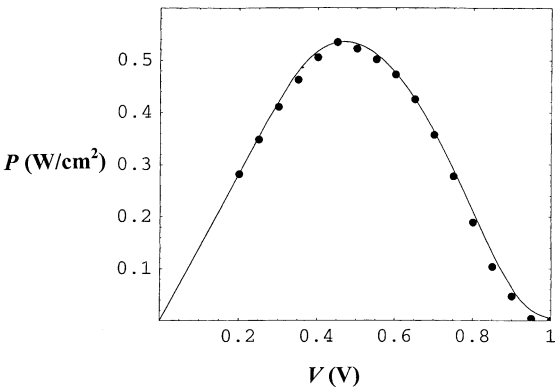

Fig. 3. Power density (W/cm^2) versus voltage (V) plot for a 5 cm^2 fuel cell operated at 80°C with a H_2/O_2 (30/30 psig) feed; humidifier temperatures of 95 and 90°C for anode and cathode, respectively; E-TEK double-sided electrodes with platinum catalyst (ω_M = 0.2 Pt on Vulcan XC-72) loading m_M = 0.4 mg Pt/cm^2 and Nafion® loading m_I = 0.7 mg/cm^2, and with a Nafion® 115 membrane.

parameter values are, therefore, not further discussed here except to observe that no additional fitted parameters were employed in applying their model of PEM conduction to the fuel cell. In addition, for the Nafion® 115 membrane used for the data here, the membrane thickness is 125 μm.

For the catalytic layers, the Pt particle size of $d_M = 2.9$ nm is taken from the particle size versus ω_M data given by Gloaguen et al. [24] and in the E-TEK catalog. The parameter $\varphi_M = 0.75$ is adopted since it provides values of catalyst dispersion consistent with the formula of Boudart [9]. For the fraction of the available metal surface in contact with ionomer, it is simply assumed that it is related to the volumetric ionomer loading in the catalyst layer q_I through the Bruggeman relation $\varphi_I = q_I^q$, with the Bruggeman exponent $q = 1.5$. The catalyst layer porosity of 0.65 assumed is in the range adopted by others.

For the HOR, the effective transfer coefficient is taken as $\vec{\alpha}_A = \frac{1}{2}$, which is commonly adopted (e.g., [6]), and the exchange-current density $i^*_{A,0,ref} = 1\,mA/cm^2$ of Pt catalyst surface at room temperature [27,37]. The effective activation energy for HOR is assumed to be $E_{A,\Phi_0} = 18$ kJ/mol [37].

As discussed above, it is found for the ORR in acid solutions that the effective transfer coefficient $\vec{\alpha}_C = 1$ at low cds, while below this voltage (high cds), frequently $\vec{\alpha}_C = \frac{1}{2}$ is observed [45,52]. Since most of the overpotential occurs at low cds, in this analysis we assume $\vec{\alpha}_C = 1$ at all cds. The change of slope may also be explained on the basis of influence of diffusion control at higher cds [3]. Further support for $\vec{\alpha}_C = 1$ is given by Parthasarathy et al. [43] determined from the Tafel slope of ORR in Nafion® electrolyte. The activation energy of ORR is assumed to be $E_{C,\Phi_0} = 76$ kJ/mol, as given by Mukerjee and Srinivasan [40]. Parthasarathy et al. [45] also provide an activation energy of $E_{C,\Phi_0} = 73$ kJ/mol. The exchange current densities for ORR reported in the literature are in the range of $i^*_{C,0,ref} = 10^{-9}$–10^{-11} A/cm^2 [33]. For example, [43] give $i^*_{C,0} = 2.2 \times 10^{-10}$ A/cm^2 for a Pt microelectrode in contact with Nafion® membrane at 298 K and 1 atm oxygen. They later revised this to $i^*_{C,0} = 8.3 \times 10^{-10}$ A/cm^2 [44]. Other values reported by this group are: $i^*_{C,0} = 3.25 \times 10^{-11}$ A/cm^2 at 30°C and $i^*_{C,0} = 3.6 \times 10^{-9}$ A/cm^2 at 80°C [45]. The above studies were with Pt microelectrode, i.e., a Pt wire was used as electrode. Thus, we adopt the value $i^*_{C,0,ref} = 10^{-11}$ at room temperature and 1 atm oxygen.

For the E-TEK gas-diffusion backing, the porosity of the carbon cloth itself is 0.78. After treatment with Teflon and carbon particles, however, its finished porosity is usually around 0.55–0.65. We assume a value of 0.65 for the treated, but uncompressed, E-TEK gas-diffusion backing. Further, the GDB thickness given is 350 μm. The final thickness of the compressed GDB in the assembled fuel cell would, however, depend upon the thickness of the gasket used as well as the torque applied. Thus, [54] assume 180 μm, while [5] assume 260 μm. The gasket thickness used by us is 250 μm. Therefore, this is the thickness assumed for the GDB. It should be mentioned that this is relatively unimportant, as the final compressed porosity and thickness are related, one compensating the other to a large extent. Thus, the final compressed porosity would be $1 - [(350/250)(1 - 0.65)] = 0.5$. The corresponding volumetric water loading in the pores, thus, is assumed to be $q_w = 0.2$ to give a final residual gas pore porosity of 0.4 as assumed by Springer et al. [54]. It should be mentioned, however, that this value likely depends upon the water supersaturation, i.e., the ratio of vapor pressure in fuel cell to that at the humidifier temperature. The residual gas pore diameter in the wetted GDB is assumed to be 2.1 μm, which is actually the only fitted parameter utilized, but is of the appropriate order [33, p. 145].

The partition coefficients of hydrogen and oxygen are taken from the literature [5]. For gas phase diffusion coefficients, we use the values calculated by Bernardi and Verbrugge [5] for 353 K, i.e., $D^0_{O_2-N_2} = pD_{O_2-N_2} = 0.279$ atm cm^2/s, $D^0_{w-O_2} = pD_{w-O_2} = 0.370$ atm cm^2/s, $D^0_{w-N_2} = pD_{w-N_2} = 0.387$ atm cm^2/s, and $D^0_{w-H_2} = pD_{w-H_2} = 1.2$ atm cm^2/s, with the following temperature correction employed: $(T/353)^{1.823}$.

It is of interest to determine if the expression for effective diffusion coefficient (Eq. (13)) obtained from the complete DGM can be simplified by dropping the viscous flow or the Knudsen diffusion terms, since in the previous models for PEM fuel cells both these transport mechanisms are usually neglected. Thus, for the case shown in Fig. 2, Eq. (13) provides an effective diffusion coefficient of oxygen through the

GDB as 0.01 cm^2/s. If the d'Arcy terms are dropped, Eq. (13) yields an effective diffusion coefficient of 0.0012 cm^2/s. If, on the other hand, the Knudsen diffusion terms are dropped, it provides a value of 0.281 cm^2/s. It is, therefore, evident that the complete dusty-gas treatment for flux through the GDB is called for. In summary, the values of the various parameters utilized in the model are adopted from the literature and, thus, provide confidence in the adequacy of the theoretical model.

6. Conclusion

The PEM fuel cell, currently a serious contender for power generation for mobile and stationary applications, is in many ways a membrane reactor, involving a composite of several reaction and membrane layers and embodying the functions of simultaneous catalytic reaction and separation. This paper draws attention to this comparison and utilizes it to develop an analytical model incorporating details of the transport and/or reaction in each layer. The transport model utilized in the various layers is the DFM, which is well-suited for describing the PEM as well as the gas-diffusion layers. The proton conductivity in the PEM is influenced by its structure, the sulfonic acid group concentration, percolation threshold, water sorption characteristics, and relative humidity. The transport of gases through the gas-diffusion backing, and hence the limiting current, is affected by its pore size, porosity, thickness, and water content. In the catalyst layers, the electrocatalytic kinetics for the hydrogen oxidation and the oxygen reduction reactions are adopted from the literature. Structural details are included such as the catalyst loading, Pt/C mass fraction, catalyst microcrystallite diameter, and ionomer loading. However, it is assumed that there are no diffusional limitations and no potential drop within the catalyst layers owing to their relative thinness. The resulting model, with parameter values adopted from the literature, captures the essential features of the fuel cell performance well except at high current densities. While it is our intention to include diffusional limitations in the catalyst layer in future work, it is noteworthy that in the range of practical interest (0.5–0.7 V), the analytical model is adequate. It should also be mentioned that the model here assumes equimolar counter-diffusion of water and hydronium ion in the PEM, which bears further investigation.

Acknowledgements

The financial support for this work provided by the H Power Corp. under Naval Surface Warfare Center (NSWC) Contract No. N00167-99-C-0002 is gratefully acknowledged. Also acknowledged are contributions of Dr. Hao Tang to this work.

References

[1] G.J.K. Acres, J.C. Frost, G.A. Hards, R.J. Potter, T.R. Ralph, D. Thompsett, G.T. Burstein, G.J. Hutchings, Catal. Today 38 (1997) 393.
[2] A.W. Adamson, A.P. Gast, Physical Chemistry of Surfaces, 6th Edition, Wiley/Interscience, New York, 1997, p. 622.
[3] J.C. Amphlett, K.A.M. Creber, J.M. Davis, R.F. Mann, B.A. Peppley, D.M. Stokes, Int. J. Hydrogen Energy 19 (1994) 131.
[4] C. Berger (Ed.), Handbook of Fuel Cell Technology, Prentice-Hall, Englewood Cliffs, NJ, 1968.
[5] D.M. Bernardi, M.W. Verbrugge, AIChE J. 37 (1991) 1151.
[6] D.M. Bernardi, M.W. Verbrugge, J. Electrochem. Soc. 139 (1992) 2477.
[7] L.J.M.J. Blomen, M.N. Mugerwa, Fuel Cell Systems, Plenum Press, New York, 1993.
[8] J.O'M. Bockris, A.K.N. Reddy, Modern Electrochemistry, Vol. 2, Plenum Press, New York, 1970.
[9] M. Boudart, G. Djéga-Mariadassou, Kinetics of Heterogeneous Catalytic Reactions, Princeton University Press, Princeton, NJ, 1984.
[10] K.A. Connors, Chemical Kinetics: The Study of Reaction Rates in Solution, VCH, New York, 1990.
[11] A. Damajanovic, in: J.O'M. Bockris, B.E. Conway (Eds.), Modern Aspects of Electrochemistry, Vol. 5, Plenum Press, New York, 1969.
[12] A. Damjanovic, V. Brusic, Electrochim. Acta 12 (1967) 615.
[13] R. Datta, R.G. Rinker, J. Catal. 95 (1985) 181.
[14] S. Dechapanichkul, Porous-walled tubular catalytic reactor separator, Ph.D. Thesis, The University of Iowa, Iowa City, 1994.
[15] A.G. Dixon, Catalysis, Vol. 14, Royal Society of Chemistry, Cambridge, UK, 1999.
[16] N. Edwards, S.R. Ellis, J.C. Frost, S.E. Golunski, A.N.J. va Kuelen, N.G. Lindewald, J.G. Reinkingh, J. Power Sourc. 71 (1998) 123.
[17] M. Enyo, in: B.E. Conway, J.O'M. Bockris, E. Yeager, S.U.M. Khan, R.E. White (Eds.), Comprehensive Treatise of Electrochemistry, Plenum Press, NewYork, 1983, p. 241.
[18] T. Erdey-Grz, Kinetics of Electrode Processes, Adam Higler, London, 1972.

[19] T.F. Fuller, Solid-polymer-electrolyte fuel cells, Ph.D. Thesis, University of California, Berkeley, CA, 1992.
[20] T.F. Fuller, J. Newman, J. Electrochem. Soc. 140 (1993) 1218.
[21] T.D. Gierke, G.E. Munn, F.C. Wilson, J. Polym. Sci. Polym. Phys. Ed. 19 (1981) 1687.
[22] T.D. Gierke, W.Y. Hsu, in: A. Eisenberg, H.L. Yeager (Eds.), Perfluorinated Ionomer Membrane, American Chemical Society, Washington, DC, 1982.
[23] S. Glasstone, K.J. Laidler, H. Eyring, The Theory of Rate Processes, McGraw-Hill, New York, 1941, p. 552.
[24] F. Gloaguen, F. Andolfatto, R. Durand, P. Ozil, J. Appl. Electrochem. 24 (1994) 863.
[25] E.R. Gonzalez, J. Electrochem. Soc. 143 (1996) L113.
[26] S. Gottesfeld, J. Pafford, J. Electrochem. Soc. 135 (1988) 2651.
[27] S. Gottesfeld, T.A. Zawodzinski, in: R. Alkire, H. Gerischer, D. Kolb, C. Tobias (Eds.), Advances in Electrochemical Science and Engineering, Vol. 5, 1998, 197.
[28] W. Grot, Encyclopedia of Polymer Science and Engineering, Vol. 16, 2nd Edition, 1989.
[29] R. Jackson, Transport in Porous Catalysts, Elsevier, Amsterdam, 1977.
[30] M. Jacoby, C&EN, June 14, 1999, p. 31.
[31] J.S. Kim, R. Datta, AIChE J. 37 (1991) 1657.
[32] J. Kim, S.M. Lee, S. Srinivasan, C.E. Chamberlin, J. Electrochem. Soc. 142 (1995) 2670.
[33] K. Kinoshita, Electrochemical Oxygen Technology, Wiley, New York, 1992.
[34] K.V. Kordesh, G.R. Simader, Fuel Cells and Their Applications, VCH, Weinheim, 1996.
[35] J. Leddy, N.E. Vanderborgh, in: J.W. Van Zee, R.E. White, K. Kinoshita, H.S. Burnery (Eds.), Proceedings of the Symposium on Diaphragms, Separators, and Ion-exchange Membranes, Vols. 13–86, The Electrochemical Society, Pennington, NJ, 1986, p. 15.
[36] J. Lipkowski, P.N. Ross, Electrocatalysis, Wiley/VCH, New York, 1998.
[37] N.M. Markovic, B.N. Grugr, P.N. Ross, J. Phys. Chem. 101 (1997) 5405.
[38] E.A. Mason, A.P. Malinauskas, Gas Transport in Porous Media: The Dusty-gas Model, Elsevier, Amsterdam, 1983, p. 142.
[39] W. Mitchell, Fuel Cells, Academic Press, New York, 1963.
[40] S. Mukerjee, S. Srinivasan, J. Electroanal. Chem. 357 (1993) 201.
[41] T.V. Nguyen, R.E. White, J. Electrochem. Soc. 140 (1993) 2178.
[42] V.A. Paganin, E.A. Ticianelli, E.R. Gonzalez, J. Appl. Electrochem. 26 (1996) 297.
[43] A. Parthasarathy, C.R. Martin, S. Srinivasan, J. Electrochem. Soc. 138 (1991) 916.
[44] A. Parthasarathy, B. Dave, S. Srinivasan, A.J. Appleby, C.R. Martin, J. Electrochem. Soc. 139 (1992) 1634.
[45] A. Parthasarathy, S. Srinivasan, A.J. Appleby, C.R. Martin, J. Electrochem. Soc. 139 (1992) 2530.
[46] P. Patil, P. Zegers, J. Power Sourc. 49 (1994) 169.
[47] M.L. Perry, J. Newman, E.J. Cairns, J. Electrochem. Soc. 145 (1998) 5.
[48] D. Raistrick, in: J.W. Van Zee, R.E. White, K. Kinoshita, H.S. Burnery (Eds.), Proceedings of the Symposium on Diaphragms, Separators, and Ion-exchange Membranes, Vols. 13–86, The Electrochemical Society, Pennington, NJ, 1986, p. 172.
[49] R.C. Reid, J.M. Prausnitz, T.K. Sherwood, The Properties of Gases and Liquids, 3rd Edition, McGraw-Hill, New York, 1977.
[50] S.J. Ridge, R.E. White, Y. Tsou, R.N. Beaver, G.A. Eisman, J. Electrochem. Soc. 136 (1989) 1902.
[51] E.B. Sepa, M.V. Vojnovic, A. Damjanovic, Electrochim. Acta 26 (1981) 781.
[52] D.B. Sepa, M.V. Vojnovic, Lj.M. Vracar, Electrochim. Acta 32 (1987) 129.
[53] T.E. Springer, M.S. Wilson, S. Gottesfeld, J. Electrochem. Soc. 140 (1993) 3513.
[54] T.E. Springer, T.A. Zawodzinski, M.S. Wilson, S. Gottesfeld, J. Electrochem. Soc. 143 (1996) 587.
[55] T.E. Springer, T. Rockward, T.A. Zawodzinski, S. Gottesfeld, J. Electrochem. Soc. 148 (2001) A11–A23.
[56] T. Thampan, S. Malhotra, H. Tang, R. Datta, J. Electrochem. Soc. 147 (2000) 3242.
[57] A.Y. Tonkovich, J.L. Zilka, M.J. LaMont, Y. Wang, R.S. Wegeng, Chem. Eng. Sci. 54 (1999) 2947.
[58] W. Vogel, J. Lundquist, P. Ross, P. Stonehart, Electrochim. Acta 20 (1975) 79.
[59] K.R. Weisbrod, S.A. Grot, N.E. Vanderborgh, in: S. Gottesfeld, G. Halpert, A. Landgrebe (Eds.), Proceedings of the First International Symposium on Proton Conducting Membrane Fuel Cells I, Vols. 23–95, The Electrochemical Society, Pennington, NJ, 1995, p. 152.
[60] M.S. Wilson, S. Gottesfeld, J. Electrochem. Soc. 139 (1992) L28.